Journal of Alloys and Compounds 1080 (2026) 190275

Contents lists available at ScienceDirect

Journal of Alloys and Compounds

journal homepage: www.elsevier.com/locate/jalcom

Research article

Structural, electronic, and magnetic properties of the hexagonal double perovskite Ba_2FeIrO_6: A combined computational and experimental investigation

P. Cândido [a], L. Bufaiçal [a], L. Ghivelder [b], Mariana Lumi Ichihara Sado [c], Alysson M.A. Silva [c], H. Fabrelli [d], E.M. Bittar [d], J.F. Carvalho [a], R.C. Santana [a], Renato B. Pontes [a,*]

[a] Instituto de Física, Universidade Federal de Goiás, 74001-970, Goiânia, GO, Brazil
[b] Instituto de Física, Universidade Federal do Rio de Janeiro, 21941-909, Rio de Janeiro, RJ, Brazil
[c] Departamento de Engenharia Mecânica, Universidade de Brasília, Brasília, 70919-970, DF, Brazil
[d] Centro Brasileiro de Pesquisas Físicas, 22290-180, Rio de Janeiro, RJ, Brazil

ARTICLE INFO

Keywords:
Hexagonal double perovskite
Density functional theory calculations
Magnetism
XRD diffraction
X-ray photoelectron spectroscopy

ABSTRACT

Hexagonal double perovskites with face-sharing octahedra represent an important class of materials in which structural connectivity strongly influences electronic and magnetic properties. In this work, the structural, magnetic, and electronic properties of Ba_2FeIrO_6 were investigated using a combined experimental and computational approach. X-ray powder diffraction confirms the formation of a 6H-type hexagonal structure (space group $P6_3/mmc$), characterized by face-sharing BO_6 octahedral dimers. Investigation of the surface electronic configuration by means of X-ray photoelectron spectroscopy suggest the presence of Fe^{3+}/Fe^{2+} and Ir^{5+}/Ir^{4+} mixed valence states, while ac and dc magnetic measurements reveal a low-temperature transition at $T_C \simeq 5.0$ K with ferrimagnetic-like behavior, supported by DFT+U calculations that indicate an uncompensated antiferromagnetic ground state. Electrical resistivity measurements suggest semiconducting behavior with an activation energy of 0.24 eV. Contrastingly, electronic structure calculations consistently indicate a metallic ground state. The discrepancy between the experimental and theoretical results is discussed in terms of possible grain boundary effects in the polycrystalline sample, and/or limitations in the computational model. The metallic behavior is further rationalized by the 6H hexagonal topology, where face-sharing geometry enhances direct d–d orbital overlap and promotes electronic delocalization. These results demonstrate the strong influence of structural connectivity on the physical properties of Ba_2FeIrO_6, highlighting the role of $3d$–$5d$ interactions in hexagonal double perovskites and providing insight for the design of related functional oxide materials.

1. Introduction

In condensed matter physics and materials science, the perovskite family, characterized by its archetypal ABX_3 structure, has garnered sustained attention due to an extraordinary breadth of tunable physical properties, ranging from ferroelectricity and magnetism to superconductivity and high-efficiency photovoltaics [1–4]. This structural versatility permits the integration of diverse elemental compositions at the A, B, and X sites, thus opening up extensive possibilities for discovering materials with optimized properties. Among the various subclasses, oxide perovskites (where $X = O^{2-}$) are particularly renowned for their robust structures and stability, making them critical for applications in high-temperature catalysis, fuel cells, and spintronic devices [5–7]. The ordered substitution of the B-site cation results in the oxide double perovskite family, $A_2B'B''O_6$. This structural ordering at the B-site introduces an additional degree of freedom for tailoring electronic and magnetic interactions, often yielding emergent phenomena not observed in their single-B-site counterparts. Notable examples include half-metallic ferromagnets like Sr_2FeMoO_6 [8] and multiferroics [9], underscoring their importance in functional material design [10].

While the most commonly recognized perovskite structure is the cubic *Pm-3m* symmetry, many perovskite-related compounds adopt lower-symmetry space groups, including orthorhombic, tetragonal, and crucially, hexagonal variants [11]. Hexagonal oxide perovskites possess a particular structural design (e.g., $A_3B'B''B''O_9$ or $A_2B'B''O_6$ with hexagonal symmetry), identified through the presence of face-sharing BO_6 octahedra, distinguishing them from the ubiquitous corner-sharing

* Corresponding author.
E-mail address: pontes@ufg.br (R.B. Pontes).

https://doi.org/10.1016/j.jallcom.2026.190275
Received 30 March 2026; Received in revised form 31 July 2026; Accepted 4 August 2026
Available online 14 August 2026

connectivity of cubic perovskites [12,13]. This face-sharing arrangement leads to significantly shorter B-B interatomic distances and altered B-O-B bond angles, profoundly influencing orbital overlap and electronic correlations. The stacking sequence of the A-O_3 layers along the c-axis also differentiates hexagonal polytypes (e.g., 2H, 4H, 6H), providing additional structural complexity and opportunities for property modulation. This intricate interplay between local coordination and long-range stacking often leads to unique electronic and magnetic properties not found in their corner-sharing counterparts, as highlighted in comprehensive reviews on hexagonal perovskites as quantum materials [14]. Furthermore, the presence of heavy transition-metal (TM) ions at the B-sites can introduce strong spin–orbit coupling, leading to topologically nontrivial electronic states or unusual magnetic anisotropy, as observed in materials with complex mixed-metal-cation trimers [15]. Beyond their fascinating magnetic properties, these unique structures can also facilitate high oxide ion conductivity [16], opening new directions in the design of solid electrolytes for energy applications by exploiting induced interstitial defects and specific stacking sequences [17–20].

Within this context, the perovskite Ba_2FeIrO_6 (BFIO) emerges as a material of particular interest. Unlike many Ir-based double perovskites that adopt cubic structures [21–23], Ba_2FeIrO_6 is reported to crystallize in a hexagonal structure, a crucial factor distinguishing its properties [24]. This hexagonal phase is frequently accompanied by a notable degree of antisite disorder between the Fe and Ir cations, adding complexity to its fundamental interactions. The combination of a 3d TM ($Fe^{3+}, 3d^5$) with a 5d TM ($Ir^{5+}, 5d^4$) is particularly promising for investigating the intricate interplay between strong electron–electron correlations and the significant spin–orbit coupling inherent to the 5d Ir^{5+} ions [25]. Preliminary investigations non-peer reviewed suggest that Ba_2FeIrO_6 exhibits complex magnetic behavior at low temperatures, with evidence of a glassy phase, pointing to competing interactions and potential magnetic frustration resulting from its hexagonal structure and the mixing of Fe and Ir spins [24]. Therefore, understanding the structure–property relationships in hexagonal double perovskites like Ba_2FeIrO_6 is essential for designing advanced quantum materials with tailored electronic and magnetic properties.

Thus, this manuscript aims to describe the synthesis and structural determination of a hexagonal Ba_2FeIrO_6 double perovskite, primarily utilizing X-ray powder diffraction (XRD). This is coupled with a detailed investigation of its physical properties, specifically its electronic and magnetic structures through X-ray photoelectron spectroscopy (XPS) and magnetization measurements as a function of magnetic field [M(H)] and temperature [M(T)] and its electrical transport properties. Furthermore, first-principles calculations within the density functional theory (DFT) framework are employed to elucidate the fundamental mechanisms governing its unique magnetic and electronic features.

2. Methods

This section details the experimental and computational procedures employed to investigate the structural, magnetic, and optical properties of hexagonal Ba_2FeIrO_6 double perovskite. All materials synthesis, characterization techniques, and theoretical calculations are described herein.

2.1. Experimental details

A polycrystalline sample of Ba_2FeIrO_6 was produced by solid state reaction. Stoichiometric amounts of $BaCO_3$, Fe_2O_3 and Ir powder were ground and heated in air atmosphere at 900 °C for 24 h and at 1100 °C for another 24 h, with intermediate grinding. The resulting powder was then ground, pressed into pellet and sent to a final step of 1200 °C for 48 h. After this procedure, a dark black disk of ~10 mm diameter × ~1.5 mm thickness was obtained. The formation of the intended crystal and its structural characterization were carried out by means of room temperature X ray powder diffraction (XRD) using a Bruker D8 Discover diffractometer, operating with Cu K_α radiation. The XRD data was taken over the angular range $10° \leq 2\theta \leq 90°$, with a 2θ step size of 0.01°. Rietveld refinement was performed using GSAS software and its graphical interface program [26].

High-resolution X-ray photoelectron spectroscopy (XPS) measurements were carried out using a Thermo Scientific K-Alpha spectrometer equipped with a monochromatic Al K_α X-ray source ($h\nu$ = 1486.6 eV). Initially, survey spectra were acquired to verify the elemental composition, followed by high-resolution spectra of the Fe 2p and Ir 4f core levels. Charge neutralization was performed using the built-in dual electron/ion flood gun. The binding energy scale was referenced to the adventitious C 1s peak at 284.8 eV. Peak fitting was performed using Thermo Avantage software after Shirley background subtraction employing mixed Gaussian–Lorentzian (GL) line shapes. For the Ir 4f region, the spin–orbit splitting, area ratio and full width at half maximum (FWHM) were constrained according to the intrinsic characteristics of the doublet in order to avoid non-physical fitting solutions. Owing to the intrinsic multiplet splitting and shake-up satellite structure of the Fe 2p spectrum, the fitting procedure considered all characteristic spectral contributions to obtain the most reliable deconvolution of the mixed oxidation states.

The ac and dc magnetization measurements were carried out using Quantum Design Physical Property Measurement System (PPMS) equipments. The dc magnetization as a function of temperature [$M(T)$] was measured in both zero field cooled (ZFC) and field cooled (FC) modes. For the ZFC mode, the sample was cooled down to 2 K in absence of external field (H), then H = 1000 Oe was applied and, subsequently, the magnetization was captured with increasing temperature. For the FC mode, the H = 1000 Oe was applied at the paramagnetic state (400 K), then the system was cooled down to 2 K, and subsequently the magnetization was picked up with increasing temperature. The magnetization as a function of H [$M(H)$] was measured at 2 K, after ZFC the sample. For the ac magnetization measurement were also carried in both ZFC and FC modes, using distinct frequencies in the range 100–1000 Hz, and ac driving fields in the range 5–15 Oe. The data were recorded in two modes: (i) with a continuous temperature sweep, (ii) stabilizing the temperature at each measurement point.

2.2. Computational details

To investigate Ba_2FeIrO_6, DFT calculations were performed using the software Vienna Ab-initio Simulation Package (VASP) [27], employing the projector augmented wave (PAW) method [28] with the following valence electron configurations: Ba ($5s^25p^66s^2$), Fe ($3d^74s^1$), Ir ($5d^86s^1$), and O ($2s^22p^4$). The Perdew–Burke–Ernzerhof (PBE) formulation [29] was used for the exchange–correlation functional. In the calculations, a plane-wave cutoff energy of 600 eV was employed. The k-space Brillouin zone was sampled with a (5 × 5 × 5) Γ-centered grid. The lattice parameters and atomic positions were relaxed until the residual forces on the atoms were smaller than 0.001 eV/Å and the convergence criterion for electronic iterations was set to 1×10^{-6} eV. Strong Coulomb correlations were treated by the DFT+U approach [30] applied to the Fe-3d and Ir-5d orbitals. We investigated several combinations of Coulomb (U) and exchange (J) parameters (values in eV): (i) U_{Fe} = 5.00, J_{Fe} = 0.96 and U_{Ir} = 1.40, J_{Ir} = 0.50; (ii) U_{Fe} = 5.00, J_{Fe} = 0.96 and U_{Ir} = 1.40, J_{Ir} = 0.96; (iii) U_{Fe} = 7.00, J_{Fe} = 1.00 and U_{Ir} = 1.50, J_{Ir} = 0.50; and (iv) U_{Fe} = 8.00, J_{Fe} = 1.00 and U_{Ir} = 1.50, J_{Ir} = 0.50. The choice of these parameters was guided by previous studies of Saad H.-E. and Abdelhalim on similar double perovskite systems [31,32]. Given that the strong spin–orbit coupling typical of 5d Ir orbitals is crucial for the electronic and magnetic ground states, we extended our calculations to include SOC effects (DFT+SOC+U). Additional results obtained with the LDA [33] and SCAN meta-GGA [34] functionals are available in the Supplementary Material.

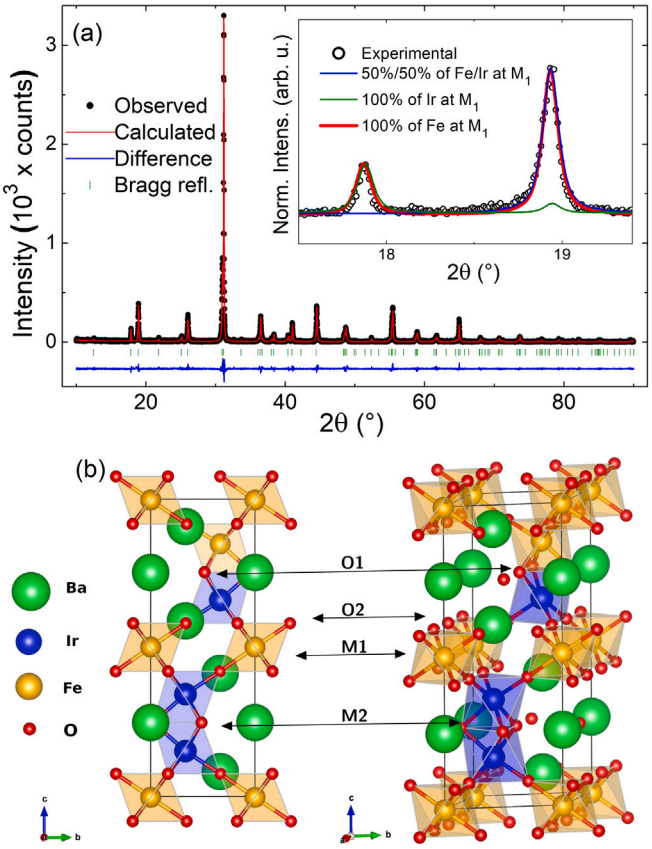

Fig. 1. (a) Rietveld refinement fitting of the XRD within the $P6_3/mmc$ space group. The inset shows a magnified view of the 17.5°–19.4° region of the experimental data, together with simulated patterns of $P6_3/mmc$ space group with different degrees of Fe/Ir occupancies in the M_1/M_2 sites. (b) Schematic representation of the $6H$ crystal structure of Ba_2FeIrO_6.

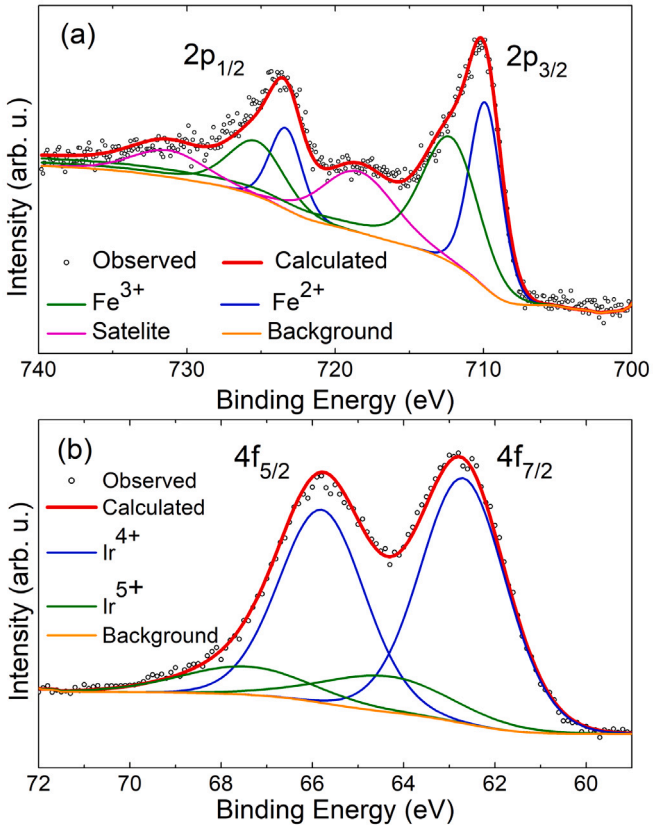

Fig. 2. The XPS spectra on Ba_2FeIrO_6 for (a) Fe $2p$ and (b) Ir $4f$.

3. Results and discussion

3.1. Experimental results

Fig. 1(a) shows the room temperature XRD pattern of Ba_2FeIrO_6, from which the crystal structure could be well refined within a 6-layered hexagonal ($6H$) crystal structure having space group $P6_3/mmc$, and no trace of secondary phases was detected. This crystal symmetry matches with that of $BaFe_{0.4}Ir_{0.6}O_3$ and other similar Ba- and Ir-based perovskites [35–38]. On this structure, shown in Fig. 1(b), one transition-metal (TM)-ion site (M_1) is surrounded by a corner-sharing octahedrum of oxygens, while the other TM-site (M_2) is enclosed by oxygens forming dimmers of face- and corner-sharing octahedra [15].

An important issue regarding the physical properties of double-perovskites is about the occupation of the TM-ion sites. This is of particular interest in the case of Ba_2FeIrO_6 compound because both Fe and Ir are anticipated to present the same stoichiometry on it, while for the dimmer-based $6H$ perovskites the M_1 and M_2 sites have different multiplicities (2 and 4, respectively), meaning that at least one of the crystallographic sites will necessarily accommodate the two TM ions. Therefore, prior to the Rietveld refinement, we simulated XRD patterns with distinct degrees of Fe/Ir occupancies at the M_1/M_2 sites. The inset of Fig. 1(a) compares some selected simulations with the observed pattern. As can be seen, the best match is the one on which the M_1 site is fully occupied by Fe, while M_2 hosts both Fe and Ir ions. Therefore, this was the starting point for our investigation. Though, the best refinement indicates that ~5% of the M_1 site is occupied by Ir, also yielding $a = b = 5.7432(1)$ Å, $c = 14.1951(4)$ Å, and $\chi^2 = 1.3$, $R_p = 12.4\%$ for the reliability parameters. Attempts to refine the O-site occupancies yielded values close to unity. Therefore, considering the limited sensitivity of Cu-K_α XRD to oxygen stoichiometry due to the low scattering factor of oxygen, the O-sites were assumed to be fully occupied. The resulting Crystallographic Information File (CIF), containing the atomic positions, was used to initialize the DFT calculations.

To investigate the surface electronic structure of Ba_2FeIrO_6, high-resolution XPS spectra of the Fe $2p$ and Ir $4f$ core levels were analyzed, as shown in Fig. 2. The Fe $2p$ spectrum exhibits the characteristic spin–orbit doublet together with pronounced shake-up satellite features typical of TM oxides. The asymmetric spectral envelope clearly indicates that the spectrum cannot be described by a single oxidation state. After deconvolution, two chemically distinct contributions corresponding to Fe^{2+} and Fe^{3+} were identified [39–41]. Considering the intrinsic complexity of the Fe $2p$ region, which is strongly influenced by multiplet splitting, charge-transfer effects and satellite structures, the fitting was performed under physically constrained conditions in order to minimize non-unique solutions, resulting in a Fe^{3+}/Fe^{2+} atomic ratio of approximately 60:40.

The Ir $4f$ XPS spectrum presents well-defined Ir $4f_{7/2}$ and Ir $4f_{5/2}$ spin–orbit components, as shown in Fig. 2(b). Owing to the relatively simple spectral structure of the Ir $4f$ region compared with Fe $2p$, the oxidation-state assignment is considerably more reliable, supporting the existence of mixed-valence iridium ions within the near-surface region [42,43]. The peak fitting yields a Ir^{4+}/Ir^{5+} ratio of approximately 80:20.

Interestingly, these findings contrast with previous investigations of the resemblant double perovskites $(Ca,Sr)_2FeIrO_6$, on which a nearly Fe^{3+}/Ir^{5+} electronic configuration was observed [44–46]. For the extensively studied half-metallic FeMo-based double perovskites, early

investigations of $(Ba,Sr,Ca)_2FeMoO_6$ demonstrated that Fe predominantly adopts a trivalent oxidation state when the A-site is occupied by the smaller Ca^{2+} and Sr^{2+} ions. In contrast, the larger ionic radius of Ba^{2+} promotes a tendency toward Fe^{2+} formation, although a significant fraction of Fe^{3+} ions remains present [47,48]. Our results for Ba_2FeIrO_6, together with previous reports on the isovalent Ca^{2+} and Sr^{2+} substitutions, suggest that a similar trend may occur in FeIr-based double perovskites.

In this context, the simultaneous observation of Fe^{2+}/Fe^{3+} and Ir^{4+}/Ir^{5+} demonstrates that Ba_2FeIrO_6 exhibits an electronically heterogeneous surface characterized by mixed-valence states. Rather than representing isolated chemical defects, these oxidation states indicate the occurrence of local electronic charge redistribution within the double-perovskite lattice. Such redistribution is commonly associated with subtle deviations from the ideal local environment, including lattice distortions, anti-site disorder between transition-metal cations and slight departures from perfect oxygen stoichiometry. Although the present XPS measurements do not allow direct quantification of oxygen vacancies, the coexistence of multiple oxidation states is fully consistent with local charge-compensation mechanisms frequently reported for complex transition-metal oxides.

This interpretation is in excellent agreement with the structural characterization presented in this work. The hexagonal crystal structure confirmed by Rietveld refinement suggests that the local coordination environment around the transition-metal ions is not perfectly uniform. Such local structural distortions modify the crystal field surrounding Fe and Ir ions, promoting partial electronic redistribution without necessarily changing the long-range crystallographic symmetry detected by X-ray diffraction. Consequently, the mixed-valence configuration observed by XPS can be regarded as the electronic manifestation of these local structural distortions.

It should be emphasized that caution is required when interpreting the TM valences estimated from XPS measurements on bulk samples. Although this technique provides valuable information regarding local electronic compensation mechanisms that are often inaccessible by bulk characterization, it probes only the outermost few nanometers of the material, with the estimated oxidation states representing the near-surface electronic configuration. TM oxides are well known to exhibit surface effects. For instance, a detailed investigation of the Fe oxidation state in $Ba_2Ca_{0.67}Fe_{0.33}NbO_{6-\delta}$ revealed that the concentration of Fe^{2+} in the near-surface region is approximately three times higher than that in the bulk [41]. Nevertheless, the present results provide evidence for mixed oxidation states of both Fe and Ir in Ba_2FeIrO_6, at least within the surface and near-surface regions probed by XPS.

Fig. 3(a) shows the ZFC-FC $M(T)$ curves, measured from 2 K to 400 K with $H = 1000$ Oe. Both curves exhibit paramagnetic (PM) behavior for a large temperature-interval. However, a sharp peak is clearly noticed at low temperatures in the ZFC curve, as typically found in antiferromagnetic (AFM) systems. On the other hand, the FC magnetization continuously increases down to the lowest measured temperature, with a bifurcation between the curves starting to develop below ~20 K. These features suggest that the AFM coupling is uncompensated, possibly related to the presence of distinct magnetic moments in the system and/or due to spin-canting.

The reciprocal magnetic susceptibility (χ^{-1}) dependence with temperature, depicted at the inset of Fig. 3(a), reveals a deflection at the PM region that signals to a deviation from the Curie–Weiss (CW) behavior. Taking into account a possible non-negligible spin–orbit coupling on Ir, a Van Vleck constant χ_0 was added to the CW equation in attempt to fit the PM region of the curve [17,49,50], resulting in the following:

$$\chi = \chi_0 + \frac{C}{T - \theta_{CW}}, \tag{1}$$

where θ_{CW} is the CW-temperature and $C = \mu_{eff}^2/8$ is the Curie constant ($\mu_{eff} = g\sqrt{S(S+1)}$ is the effective magnetic moment). The best fit of the PM region yields $\theta_{CW} \simeq -5.9$ K, $\chi_0 \simeq 1.2 \times 10^{-3}$ emu/Oe and μ_{eff}

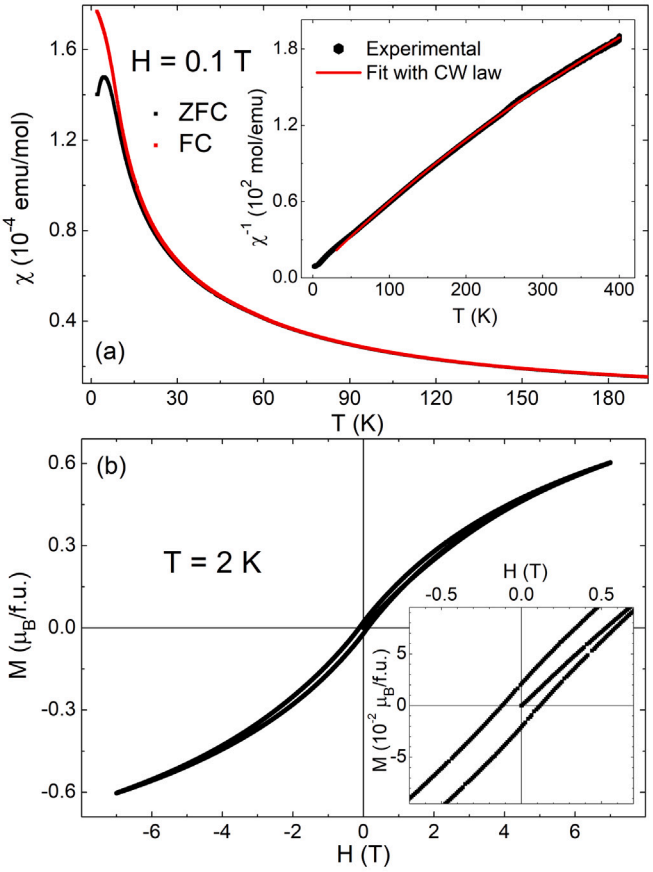

Fig. 3. (a) ZFC-FC $M(T)$ curves measured with $H = 1000$ Oe. The inset shows the ZFC χ^{-1} curve, where the straight line corresponds to best fit of PM region with the adapted CW law (see text). (b) $M(H)$ curve measured at 2 K, where the inset shows a magnified view of the low H region, highlighting the system's magnetic coercivity.

$\simeq 3.6\mu_B$/f.u. The χ_0 value is in the range usually found for Ba-based hexagonal perovskites [17,49–52], while θ_{CW} is reasonably close to the material's magnetic ordering temperature, with its negative sign endorsing the scenario of AFM interactions. The μ_{eff}, however, is significantly smaller than expected for a system presenting Fe^{3+}/Fe^{2+} [53], even if one assumes that a non-negligible SOC leads to a quenched magnetic moment for Ir^{5+} [49]. Here we recall that, contrasting to most of the double-perovskites that exhibit a 3-dimensional rock-salt arrangement for the TM ions, in our hexagonal perovskite the M_1O_6 layer and the M_2O_6 dimers form a magnetic structure of reduced dimensionality, certainly impacting the material's magnetic properties [15,54]. Furthermore, as we shall see later, our results of electrical transport signals to a very small band gap for this system, while the electronic structure calculations suggest an intrinsic metallic character. Both the low dimensionality and the delocalized character of Fe/Ir electrons are expected to contribute for the deviation from the CW law [55].

Fig. 3(b) shows the $M(H)$ curve measured for Ba_2FeIrO_6 at 2 K. Although there is no tendency of saturation typical of FM materials, the shape of the curve neither exhibits the linear behavior expected for a purely AFM system. Furthermore, a coercive field $H_C \simeq 0.12$ T is noticed at the inset of the figure. These features give further indicative of uncompensated AFM coupling that results in ferrimagnetic (FIM) behavior. From these results, however, it is not possible to determine whether this net moment comes from uncompensated interactions between two distinct TM ions, from spin-canting or even from a spin glass (SG)-like state. The use of additional techniques is paramount to unravel this issue.

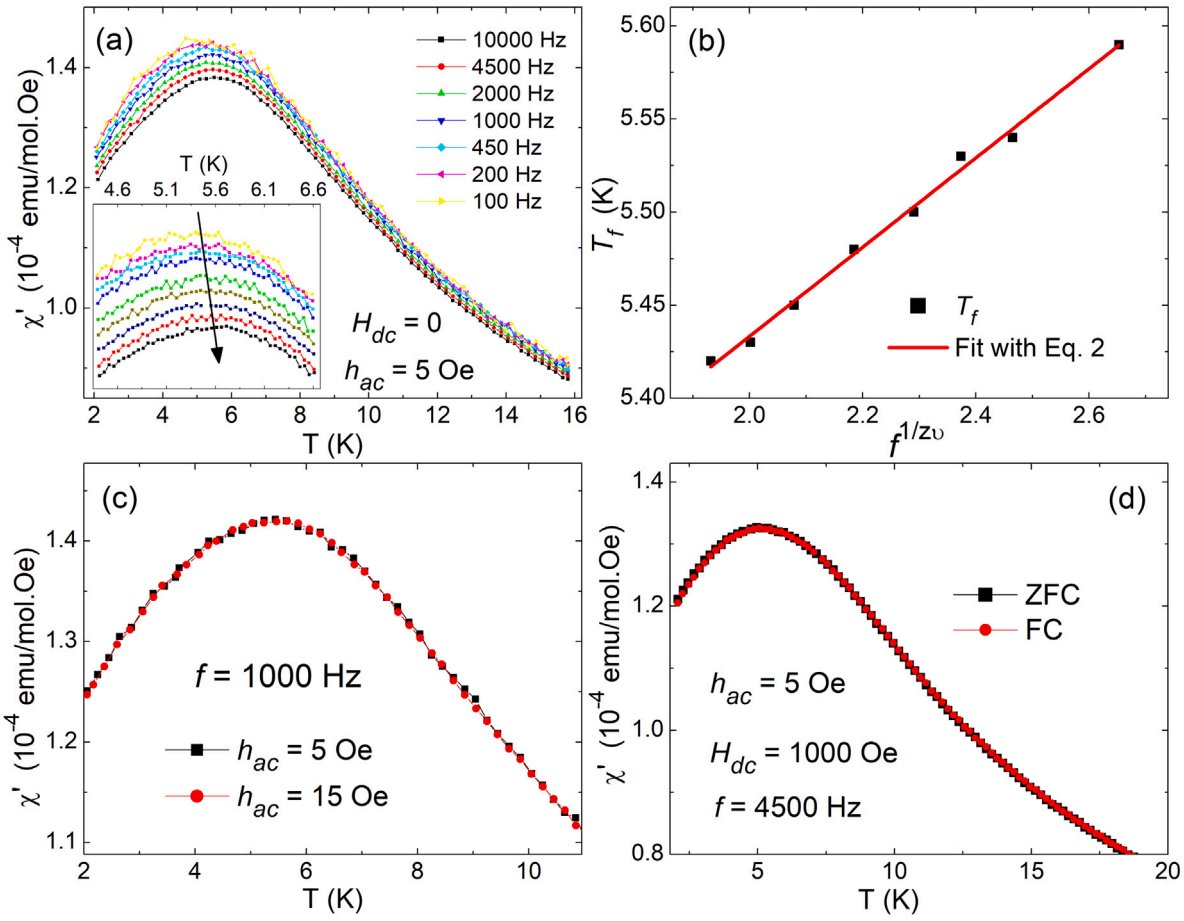

Fig. 4. (a) χ'_{ac} curves measured with the temperature varying in the sweep mode in h_{ac} = 5 Oe, f ranging from 100 to 10,000 Hz. The inset shows a magnified view of the low temperature region of eight χ'_{ac} curves for which the temperature was stabilized in each measured point. (b) T_f as a function of f, on which the straight line represents the best fit with the dynamic scaling equation. (c) χ'_{ac} curves measured with h_{ac} = 5 and 15 Oe in fixed f = 1000 Hz. (d) ZFC-FC χ'_{ac} curves measured with f = 4500 Hz and H_{dc} = 1000 Oe superimposed to h_{ac} = 5 Oe.

In order to gain further insight into the nature of the low-temperature peak observed in the ZFC dc magnetization data, we performed ac magnetic susceptibility measurements with continuous temperature sweep under an oscillating field of h_{ac} = 5 Oe and at seven excitation frequencies (f) ranging from 100 to 10,000 Hz. Fig. 4(a) depicts the real part of the ac magnetic susceptibility, χ'_{ac}. As can be seen, the peak magnitude decreases with increasing f, while a subtle shift of the peak position (T_f) toward higher temperatures is also observed. Such a frequency dependence could, at first glance, suggest the presence of a glassy magnetic state [56].

To determine the peak position more accurately, additional χ_{ac} measurements were performed at eight frequencies, with the temperature stabilized at each measurement point. A magnified view of the peak region, shown in the inset of Fig. 4(a), confirms that the f-induced shifts are indeed very small. Fig. 4(b) shows the dependence of T_f on f, together with the best fit obtained using the critical slowing down equation of the dynamic scaling theory, commonly employed for glassy magnetic systems [57]

$$\frac{\tau}{\tau_0} = \left[\frac{(T_f - T_C)}{T_C}\right]^{-z\nu}, \qquad (2)$$

where T_C is the transition temperature (corresponding to the limiting value of T_f as $f \to 0$), $z\nu$ is the dynamic critical exponent, and τ_0 is the microscopic relaxation time. The fit yields $T_C \simeq 5.0$ K, $z\nu \simeq 9.4$ and $\tau_0 \simeq 6.1 \times 10^{-14}$ s. Such a small value for the characteristic relaxation time is generally associated with the relaxation of individuals, or only weakly interacting, magnetic moments rather than with the cooperative dynamics characteristic of SG-like states [58].

To further investigate the magnetic dynamics, ac susceptibility measurements were also performed at a fixed frequency of f = 1000 Hz while varying the excitation field amplitude from h_{ac} = 5 to 15 Oe. The resulting χ'_{ac} curves divided by the driving field, shown in Fig. 4(c), exhibit an almost complete overlap. This linear response for such large driving fields differs from that typically observed in SG systems, which generally display a significant dependence on the excitation field amplitude, and is instead more consistent with AFM ordering [56].

Finally, ZFC and FC ac susceptibility measurements were carried out under a superimposed dc magnetic field of H_{dc} = 0.1 T and an ac excitation field of h_{ac} = 5 Oe. The resulting curves, shown in Fig. 4(d), nearly coincide over the entire temperature range investigated. Once again, this behavior is inconsistent with the presence of a conventional glassy magnetic state. Therefore, although complementary microscopic probes, such as muon spin spectroscopy and neutron powder diffraction, are still required for a definitive determination of the magnetic ground state of Ba_2FeIrO_6, the present results strongly suggest that the peak detected in the magnetization measurements is associated with AFM ordering, from which the weak frequency dependence observed in the ac susceptibility may arise from a small fraction of slowly fluctuating individual magnetic moments related to cation disorder and/or grain-boundary effects. These moments appear to be sufficiently dilute or weakly coupled that they do not develop the cooperative dynamics typically expected for a SG phase.

The electrical resistivity (ρ) was measured from 400 K down to ~20 K, below which the resistance achieved the limit of detection of the equipment. Qualitatively, the shape of the curve shown in Fig.

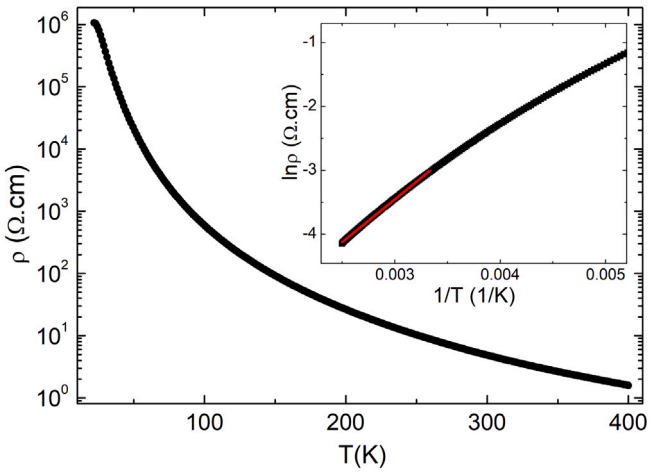

Fig. 5. Temperature dependence of ρ. The inset shows the fit of the high temperature region of the curve with the thermally activated model.

5 suggests a semiconducting/insulating-like behavior. Therefore, the thermally activated mechanism was checked out by fitting the high temperature region of the curve with the Arrhenius law:

$$ln\rho = ln\rho_0 + E_G/k_BT, \tag{3}$$

where ρ_0 is a pre-exponential factor, k_B is the Boltzmann constant and E_G is the activated band gap. The best fit, depicted at the inset of Fig. 5, yields $\rho_0 \simeq 6 \times 10^{-4}$ Ωcm and $E_G \simeq 0.24$ eV, which is smaller than values usually found for insulators or even semiconductors [59]. Here we recall the polycrystalline character of the sample here investigated. In polycrystalline double perovskites, the highly defective nature of the grain's surface may preclude the electronic transport through the grain boundaries even when the core is metallic [60]. Hence, one cannot rule out a scenario where Ba_2FeIrO_6 is intrinsically metallic, with grain boundaries effects being responsible for its apparent insulating character.

3.2. DFT-based results

Before analyzing the DFT results, the Goldschmidt tolerance factor (f) [61], shown in Table 1, was calculated using the following equation:

$$f = \frac{R_{Ba} + R_O}{\sqrt{2}\left((R_{Fe}/2) + (R_{Ir}/2) + R_O\right)}. \tag{4}$$

To determine the effective ionic radii (R_{Fe} and R_{Ir}), we utilized Shannon's tables [62] alongside the mixed oxidation states obtained from X-ray photoelectron spectroscopy (XPS) measurements. The individual ionic radii used for the fixed lattice sites were $R_{Ba^{2+}} = 1.61$ Å and $R_{O^{2-}} = 1.35$ Å, while the iridium species were taken as $R_{Ir^{4+}} = 0.625$ Å and $R_{Ir^{5+}} = 0.57$ Å. For the iron species, the radii depend heavily on the spin state: $R_{Fe^{3+}} = 0.645$ Å [High-Spin (HS)] or 0.55 Å [Low-Spin (LS)], and $R_{Fe^{2+}} = 0.78$ Å (HS) or 0.61 Å (LS). According to the XPS data, the Ir site was modeled with a weighted proportion of 80% Ir^{4+} and 20% Ir^{5+}. For the Fe site, two possible configurations were evaluated to compute the weighted average radius: (i) 60% Fe^{3+} (LS) and 40% Fe^{2+} (LS), and (ii) 60% Fe^{3+} (HS) and 40% Fe^{2+} (HS). Using these explicit radii and proportions, the calculations yield $f = 1.08$ for the LS case and $f = 1.04$ for the HS case. Generally, for double perovskites, a tolerance factor of $f > 1.0$ indicates a hexagonal structure [10,63], which perfectly aligns with the XRD measurements presented in this work.

Comparing the DFT and experimental results of the structural properties [see Table 1], it is possible to observe good agreement regarding the structural parameters. The deviation between the experimental values and the DFT results is approximately 0.7% for a and b, and 0.63% for c. Regarding the bond angles, the angle associated with the corner-sharing oxygen (O2) is close to 180° in both experimental and DFT calculations, as expected. However, the bond angle associated with the face-sharing oxygen (O1) disagrees with the value of 70.5° reported in the literature [15]. Instead, both our experimental and DFT results indicate an angle closer to 90°. These wider bond angles lead to an increased distance between the TM ions, which can have a significant impact on the physical properties of Ba_2FeIrO_6. A comparison between the bond distances of the theoretical cubic Ba_2FeIrO_6 reported in the literature [31] (Fe–O = 2.02 Å and Ir–O = 1.98 Å) and our DFT results for the hexagonal phase reveals a deviation of less than 3%.

Table 1
Comparison between experimental (XRD) and DFT (GGA-PBE) structural parameters, tolerance factor (f) for the LS (HS) states, standard enthalpy of formation, and bond lengths of Ba_2FeIrO_6.

Parameter	DFT-calc.	XDR-Exp.
Lattice Parameters and Other Properties		
a (Å)	5.78	5.74
b (Å)	5.78	5.74
c (Å)	14.28	14.19
V (Å^3)	413.48	405.50
V/Z (Å^3)	137.83	135.17
f	1.08(1.04)	–
ΔH_f° (KJ/mol)	−1729, 73	–
Bond Angles		
Ir_{M2} – O2 – Fe_{M1}	178°	175°
Fe_{M2} – O2 – Fe_{M1}	176°	175°
Ir_{M2} – O1 – Fe_{M2}	85°	90°
Ir_{M2} – O1 – Ir_{M2}	83°	90°
Bond Distances (Å)		
Ir_{M2} – O2	1.98	2.01
Fe_{M1} – O2	2.06	1.96
Ir_{M2} – O1	2.03	1.93
Fe_{M2} – O2	2.02	1.93

In addition, the standard enthalpy of the formation energy (ΔH_f°) was obtained through DFT total energies of Ba_2FeIrO_6 and its constituent elements, following the relation:

$$\Delta H_f^O = E_{Tot} - (2E_{Ba} + E_{Fe} + E_{Ir} + 6E_O), \tag{5}$$

where E_{Tot} is the total energy of the system, while E_{Ba}, E_{Fe}, E_{Ir}, and E_{O_2} correspond to the energies of bulk Ba, Fe, Ir, and the O_2 molecule, respectively. The negative value of ΔH_f^O indicates that Ba_2FeIrO_6 is thermodynamically stable.

Following the structural characterization of Ba_2FeIrO_6 double perovskite, we studied its magnetic properties. The unit cell of Ba_2FeIrO_6 contains 6 magnetic atoms (3 Fe and 3 Ir), resulting in a total of $2^6 = 64$ possible spin configurations. Among these, 20 are antiferromagnetic (AFM) configurations (defined by an equal number of up and down spins). By discarding symmetrically redundant cases, 32 unique spin configurations remain. We performed SCF calculations using the GGA functional for all the 32 unique configurations. Upon relaxation, the 32 initial configurations converged to 7 distinct magnetic states. The lowest-energy configuration is presented in Fig. 6, while the remaining configurations are shown in Supplementary Material.

Once the lowest-energy spin configuration was determined, it was necessary to apply corrections to the exchange–correlation functional. Due to the localized nature of the d electrons, the standard GGA functional is insufficient because it can lead to an over-delocalization of electrons, resulting in an incorrect description of many TM oxides with strongly localized d electrons [34]. Therefore, calculations were performed using the DFT+U method with several U values, as described in the Computational Details. We report here the results obtained with $U_{Fe} = 5.00$ eV, $J_{Fe} = 0.96$ eV and $U_{Ir} = 1.40$ eV, $J_{Ir} = 0.50$ eV. This choice

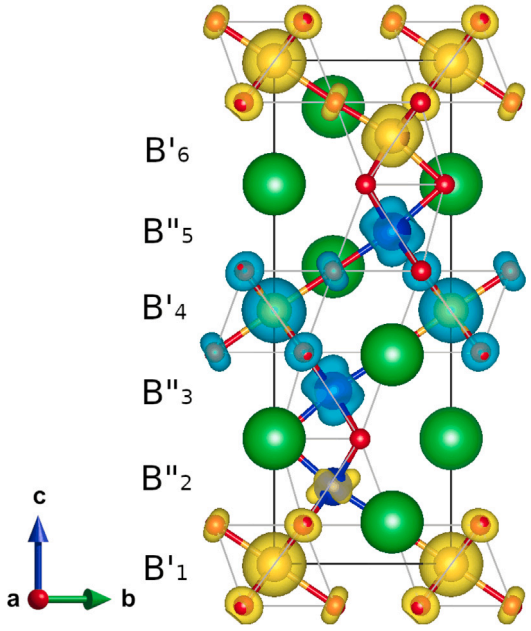

Fig. 6. Isosurface of spin magnetization density at 0.02 $e/\mathring{A}^3$ with yellow for spin-up and blue for spin-down.

is justified because the electronic band structure remained qualitatively similar upon varying U, as demonstrated in the electronic properties section and will be discussed in greater depth in the next section.

To investigate the origin of the observed uncompensated antiferromagnetic (AFM) coupling, we explored the possibility of spin canting using DFT calculations with spin–orbit coupling (SOC). To assess the stability of the magnetic ground state, we compared the total energies of a constrained collinear configuration along the z-axis (E_z) and a relaxed non-collinear setup (E_{ncl}) initialized with off-axis components. Our results indicate that the collinear ferrimagnetic order is energetically more favorable, with the z-aligned state being lower in energy by:

$$\Delta E = E_{ncl} - E_z \approx 3.02\,\text{meV}. \quad (6)$$

All magnetic calculations were performed using the optimized geometry obtained from the initial collinear relaxation. To ensure that the energy difference $\Delta E = 3.02$ meV is strictly attributed to magnetic anisotropy and non-collinear effects, the ionic positions and cell parameters were kept fixed in both the z-aligned and the relaxed non-collinear runs. Although a subtle spin canting cannot be entirely ruled out in experimental polycrystalline samples due to local structural distortions or thermal fluctuations, it does not alter the fundamental electronic conclusions of this study. For completeness, a table containing the calculated local magnetic moments for the relaxed non-collinear conformation is provided in the Supplementary Material. Hereafter, we proceed with the discussion focusing on the lower-energy collinear configuration.

From Table 2, it is also evident that the magnetic moment of the Fe atoms is sensitive to the Hubbard U parameter, while the Ir moments are much more sensitive to spin–orbit coupling (SOC), as expected. A similar behavior is observed in the cubic counterpart, despite the fact that the cubic phase is ferromagnetic [31]. Also, as tabulated in Table 2, the calculated local magnetic moments for Ba_2FeIrO_6 exhibit a pronounced site-dependence. Within the GGA+SOC+U framework, the Fe sites in corner-sharing octahedra (B_1' and B_4') exhibit spin moments of approximately 4.14 and −4.16 μ_B, consistent with a high-spin configuration modulated by Fe($3d$)–O($2p$) hybridization. In contrast, the B_6' site shows a significantly suppressed Fe spin moment of 3.69 μ_B, which we attribute to the enhanced direct d–d orbital overlap and electronic

Table 2
Calculated spin magnetic moments (orbital moments) [in μ_B] of B'(Fe), B"(Ir) and two oxygen atoms. The sites shown in Fig. 6.

Site	GGA	GGA+U	GGA+SOC	GGA+SOC+U
B_1'(Fe)	3.57	4.14	3.58	4.14(0.07)
B_2"(Ir)	0.48	0.35	0.43	0.43 (0.12)
B_3"(Ir)	−0.86	−0.86	−0.65	−0.55(−0.11)
B_4'(Fe)	−3.75	−4.14	−3.77	−4.16(−0.07)
B_5"(Ir)	−0.92	−1.11	−0.72	−0.86(−0.08)
B_6'(Fe)	2.37	3.73	2.33	3.69(0.02)
O1	−0.04	−0.08	−0.03	−0.06
O2	−0.23	−0.19	−0.19	−0.18
Total mom.	0.48	0.55	0.96	2.26(−0.10)

delocalization characteristic of the face-sharing geometry. The Ir spin moments are notably lower (0.43, −0.55, and −0.86 μ_B), indicating the presence of low-spin d^4 state where the interplay between strong SOC and local trigonal distortions leads to a nearly non-magnetic $J_{\text{eff}} = 0$ ground state.

Regarding the orbital contribution, the moments at the Fe sites (0.07, −0.07, and 0.02 μ_B) are nearly quenched, as expected for a half-filled d-shell. In contrast, the Ir sites display substantially larger orbital moments (0.12, −0.11, and −0.08 μ_B), reflecting the much stronger spin–orbit coupling of the 5d states. Across all sites, the orbital moments are coupled parallel to their respective spin moments. This complex coexistence of positive and negative local moments confirms a ferrimagnetic (FiM) ordering with a net total moment of 2.26 μ_B per unit cell. This result clarifies the origin of the net magnetism as arising from the inequivalence of magnetic moment magnitudes on different sites (uncompensated AFM coupling) rather than spin-canting, showing excellent agreement with our experimental data.

To investigate the electronic structure of the Ba_2FeIrO_6 double perovskite in detail, Fig. 7 presents the band structure and density of states (DOS) calculated using GGA-PBE, GGA+U, and GGA+SOC+U. The parameters were set to $U_{\text{Fe}} = 5.00$ eV ($J_{\text{Fe}} = 0.96$ eV) and $U_{\text{Ir}} = 1.40$ eV ($J_{\text{Ir}} = 0.50$ eV). The high-symmetry path used for these calculations is illustrated in Fig. 7(d) and was consistently applied throughout this work. Figs. 7(a), (b), and (c) indicate a metallic ground state in the hexagonal Ba_2FeIrO_6, with no energy gap at the Fermi level (E_F). Near E_F, the DOS is dominated by Ir 5d and O 2p orbitals, reflecting the strong hybridization typical of hexagonal perovskites with face-sharing octahedra, while the Fe 3d states contribute significantly to the conduction band.

In contrast, previous studies on the cubic polymorph of Ba2FeIrO6 have reported half-metallic behavior [31]. The absence of such a gap in the present 6H phase highlights the critical role of structural connectivity. In particular, the face-sharing geometry is expected to broaden the electronic bands through enhanced orbital overlap, suppressing gap formation in both spin channels and stabilizing the metallic ferrimagnetic state obtained in our calculations. However, it is well known that standard GGA functionals tend to underestimate band gaps or even fail to describe Mott-insulating states. While the temperature-dependent resistivity of our polycrystalline sample suggested a small activation gap of 0.24 eV, our DFT results remain metallic even upon the inclusion of Hubbard U and SOC. Additional calculations using various U values within LDA, GGA and SCAN meta-GGA frameworks, provided in the Supplementary Material, further confirm the absence of an electronic bandgap. These results suggest that the intrinsic ground state of Ba_2FeIrO_6 is metallic, while the resistive behavior likely stems from morphological or transport-related effects.

The metallic nature of Ba2FeIrO6 can be rationalized in terms of the 6H-hexagonal topology discussed above. In this structure, the reduced metal–metal distance within the face-sharing dimers enhances direct d–d orbital overlap, which promotes increased electronic delocalization. As a consequence, the kinetic energy gain associated with electron hopping can partially counterbalance correlation-driven localization effects.

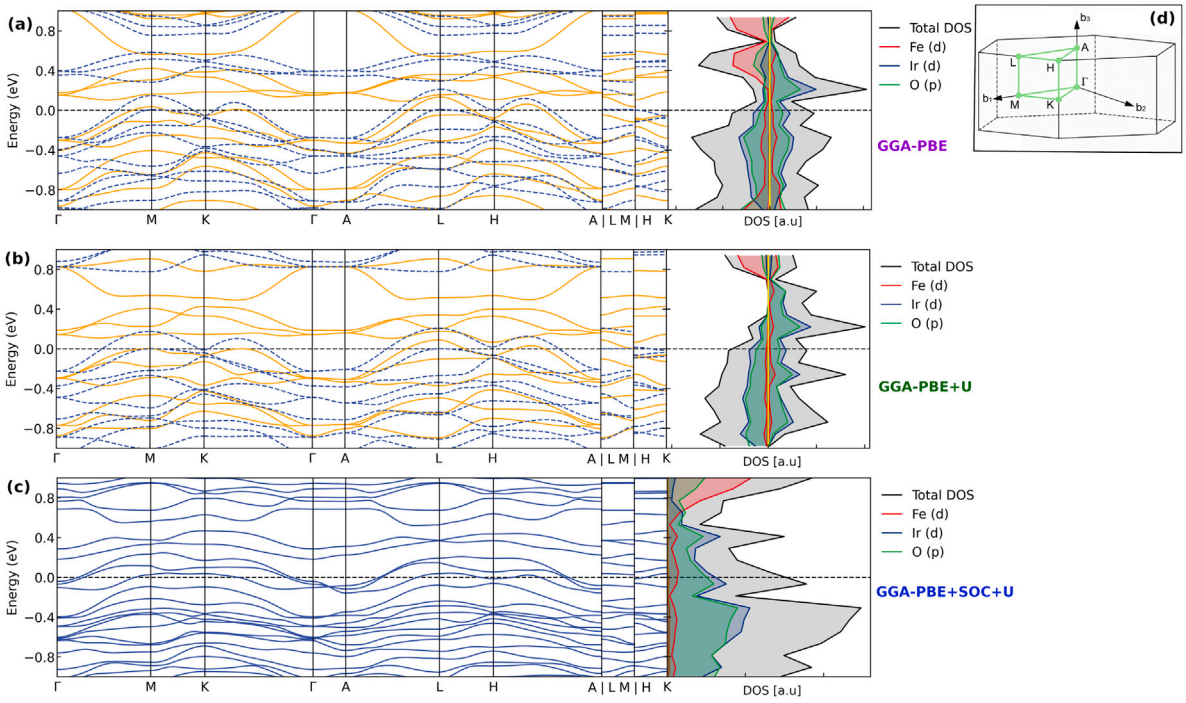

Fig. 7. Electronic band structures and corresponding density of states (DOS) calculated using: (a) GGA-PBE, (b) GGA-PBE+U, (c) GGA-PBE+SOC+U (where U_{Fe} = 5.00 eV, J_{Fe} = 0.96 eV, U_{Ir} = 1.40 eV, and J_{Ir} = 0.50 eV) and (d) The first Brillouin zone of the hexagonal lattice (black), highlighting the high-symmetry path (green) along which the electronic structure was calculated.

4. Conclusions

In summary, we have investigated the structural, magnetic, and electronic properties of the hexagonal double perovskite Ba_2FeIrO_6 through a combined experimental and computational approach. X-ray diffraction analysis confirmed that the compound, synthesized by a conventional solid-state reaction, crystallizes in a 6H-type hexagonal structure (space group $P6_3/mmc$), characterized by a sequence of face-sharing BO_6 octahedral dimers. This specific connectivity leads to Ir–O–Fe bond angles near 90°, which significantly moderates the exchange interactions compared to the more common corner-sharing cubic perovskites.

Magnetic measurements revealed a complex magnetic ground state with a transition temperature of approximately 5.0 K, most likely associated with AFM coupling between the TM ions. The observed divergence between zero-field-cooled (ZFC) and field-cooled (FC) curves, coupled with a distinct coercive field ($H_C \simeq 0.12$ T) and the characteristics of the dynamic magnetization, suggest a ferrimagnetic-like behavior, possibly associated to the presence of distinct magnetic moments along the lattice. Our DFT+U calculations successfully elucidated this state, identifying it as an uncompensated antiferromagnetic configuration. The net magnetization arises not from spin-canting, but from the site-dependent magnetic moments of Fe and Ir ions occupying different crystallographic positions ($M1$ and $M2$ sites), which do not fully cancel out.

Regarding the electronic nature of Ba_2FeIrO_6, we observed a dual behavior: while electrical transport measurements indicate a semiconducting character with activation energy of 0.24 eV, DFT band structure calculations point toward a metallic ground state. This discrepancy may be attributed to extrinsic grain boundary effects inherent in polycrystalline samples, masking the intrinsic metallic nature of the bulk. Importantly, this metallic behavior can be understood as a direct consequence of the 6H hexagonal topology, in which the face-sharing geometry enhances direct d–d orbital overlap and promotes electronic delocalization, effectively counteracting correlation-driven localization effects.

Complementing this picture, the XPS analysis reveals that the surface of Ba_2FeIrO_6 is characterized by a mixed-valence electronic structure involving both Fe and Ir ions. More importantly, when interpreted together with the XRD and magnetic measurements, the XPS results establish a coherent structure–property relationship in which local structural distortions promote electronic charge redistribution, giving rise to mixed oxidation states that ultimately govern the transport and magnetic properties of the double perovskite.

Thus, our findings highlight the critical role of face-sharing connectivity and the interplay between $3d$ (Fe) and $5d$ (Ir) orbitals in shaping the physical properties of hexagonal perovskites, establishing a clear structure–property relationship that may guide the design of related $3d$–$5d$ hexagonal oxides for spintronic and quantum material applications.

CRediT authorship contribution statement

P. Cândido: Writing – review & editing, Writing – original draft, Visualization, Validation, Software, Investigation, Formal analysis, Data curation. **L. Bufaiçal:** Writing – review & editing, Writing – original draft, Visualization, Validation, Supervision, Resources, Project administration, Methodology, Investigation, Funding acquisition, Formal analysis, Data curation, Conceptualization. **L. Ghivelder:** Data curation, Formal analysis, Investigation, Resources, Validation, Writing – review & editing. **Mariana Lumi Ichihara Sado:** Data curation, Formal analysis, Investigation, Validation, Writing – review & editing. **Alysson M.A. Silva:** Data curation, Formal analysis, Investigation, Resources, Validation, Writing – review & editing. **H. Fabrelli:** Writing – review & editing, Writing – original draft, Visualization, Validation, Investigation, Formal analysis, Data curation. **E.M. Bittar:** Writing – review & editing, Writing – original draft, Validation, Project administration, Methodology, Investigation, Formal analysis, Data curation. **J.F. Carvalho:** Data curation, Formal analysis, Investigation, Resources, Validation, Writing – review & editing. **R.C. Santana:** Writing – review & editing, Writing – original draft, Visualization, Validation, Resources, Project administration, Investigation, Formal analysis, Data curation.

Renato B. Pontes: Writing – review & editing, Writing – original draft, Visualization, Validation, Supervision, Software, Resources, Project administration, Methodology, Investigation, Funding acquisition, Formal analysis, Data curation, Conceptualization.

Declaration of competing interest

The authors declare the following financial interests/personal relationships which may be considered as potential competing interests: Renato Borges Pontes reports financial support was provided by Foundation for Research Support of Goiás State. Ricardo Costa de Santana reports financial support was provided by Foundation for Research Support of Goiás State. Pedro Candido reports financial support was provided by Coordination for the improvement of Higher Education Personnel. Leandro Bufaical reports financial support was provided by National Council for Scientific and Technological Development. Eduardo M. Bittar reports financial support was provided by National Council for Scientific and Technological Development. If there are other authors, they declare that they have no known competing financial interests or personal relationships that could have appeared to influence the work reported in this paper.

Acknowledgments

This study was financed by the Brazilian agencies CAPES/AUGM (88881.004658/2024-01), FAPEG (Grants AUX2024361000003, AUX2024301000048) and CNPq (Grant 305394/2023-1), R. B. P. and R. C. S. acknowledge financial support from CNPq/FAPEG (Grants No. 202510267001608 and No. 202510267001607). P.C. acknowledges the Brazilian agency CAPES for the scholarship. This work used computational resources of the LaMCAD/UFG, CENAPAD-SP, Coaraci Supercomputer (Fapesp grant 2019/17874-0) and the National Laboratory for Scientific Computing (LNCC/MCTI) for providing HPC resources of the SDumont supercomputer.

Appendix A. Supplementary data

Supplementary material related to this article can be found online at https://doi.org/10.1016/j.jallcom.2026.190275.

References

[1] F.S. Galasso, Structure, Properties and Preparation of Perovskite-Type Compounds: International Series of Monographs in Solid State Physics, vol. 5, Elsevier, 2013.
[2] L. Yuan, Q. Xue, F. Wang, N. Li, G.I.N. Waterhouse, C.J. Brabec, F. Gao, K. Yan, Perovskite solar cells and light emitting diodes: Materials chemistry, device physics and relationship, Chem. Rev. 125 (2025) 5057.
[3] M. Humayun, Z. Li, M. Israr, A. Khan, W. Luo, C. Wang, Z. Shao, Perovskite type ABO_3 oxides in photocatalysis, electrocatalysis, and solid oxide fuel cells: State of the art and future prospects, Chem. Rev. 125 (2025) 3165.
[4] M. Kim, G.M. McNally, H.H. Kim, et al., Superconductivity in (Ba,K)SbO_3, Nat. Mater. 21 (2022) 627.
[5] F. Tayari, S.S. Teixeira, M.P.F. Graça, K.I. Nassar, A comprehensive review of recent advances in perovskite materials: Electrical, dielectric, and magnetic properties, Inorganics 13 (2025) 67.
[6] K. Wang, C. Han, Z. Shao, J. Qiu, S. Wang, S. Liu, Perovskite oxide catalysts for advanced oxidation reactions, Adv. Funct. Mater. 31 (2021) 2102089.
[7] E. Darkaoui, S. Mouslih, J. Islah, M. Archi, A. Abbassi, S. Taj, B. Manaut, H. Ez-Zahraouy, Investigation of Ba_2SmOsO_6 and Ba_2InOsO_6 double perovskite oxide for spintronic and linear optoelectronic applications using DFT and dft+u methods, J. Magn. Magn. Mater. 622 (2025) 172980.
[8] A. Nykänen, I. Angervo, H. Huhtinen, P. Paturi, J. Phys. Condens. Matter. 37 (2025) 485701.
[9] B. Sun, G. Zhou, L. Sun, H. Zhao, Y. Chen, F. Yang, Y. Zhao, Q. Song, Nanoscale Horiz. 6 (2021) 939.
[10] S. Vasala, M. Karppinen, $A_2B'B''O_6$ perovskites: A review, Prog. Solid State Chem. 43 (2015) 1.
[11] S. Simpson, M.S. Senn, Octahedral tilting in perovskite polytypes, Chem. Mater. 37 (2025) 4524.
[12] S. Fop, K.S. McCombie, E.J. Wildman, J.M.S. Skakle, A.C. McLaughlin, Chem. Commun. 55 (2019) 2127.
[13] M.W. Lufaso, H.-C. zur Loye, Crystal structures and magnetic properties of mixed iridium-ruthenium triple perovskites. 2. $Ba_3MRuIrO_9$, (M=Li, Na, Mg, Ni, Zn, Bi, In), Inorg. Chem. 44 (2005) 9154.
[14] L.T. Nguyen, R.J. Cava, Hexagonal perovskites as quantum materials, Chem. Rev. 121 (2020) 2935.
[15] S.L. Kunz, M. Haefner, O. Clemens, "Hexagonal" perovskites: From stacking sequence to space group symmetry and new opportunities, Chem. Mater. 36 (2024) 11341.
[16] S. Fop, K.S. McCombie, E.J. Wildman, J.M.S. Skakle, A.C. McLaughlin, Nat. Mater. 19 (2020) 752.
[17] J. Chen, H.L. Feng, K. Yamaura, Review of progress in the materials development of Re, Os, and Ir-based double perovskite oxides, Mater. Today Phys. 40 (2024) 101302.
[18] M. Amores, H. El-Shinawi, I. McClelland, S.R. Yeandel, P.J. Baker, R.I. Smith, H.Y. Playford, P. Goddard, S.A. Corr, E.J. Cussen, $Li_{1.5}La_{1.5}MO_6$ (M = W^{6+}, Te^{6+}) as a new series of lithium-rich double perovskites for all-solid-state lithium-ion batteries, Nat. Commun. 11 (2020) 6392.
[19] P.S. Kuznetsova, L.R. Tarutina, A.P. Tarutin, G.K. Vdovin, D.A. Medvedev, Structural insights and proton transport features in a hexagonal $Ba_5Ho_2Al_2SnO_{13}$ perovskite, J. Eur. Ceram. Soc. 46 (2026) 118444.
[20] C. Zhou, J. Sunarso, Y. Song, J. Dai, J. Zhang, B. Gu, W. Zhou, Z. Shao, New reduced-temperature ceramic fuel cells with dual-ion conducting electrolyte and triple-conducting double perovskite cathode, J. Mater. Chem. A 7 (2019) 13265.
[21] T. Dey, A. Maljuk, D.V. Efremov, O. Kataeva, S. Gass, C.G.F. Blum, F. Steckel, D. Gruner, T. Ritschel, A.U.B. Wolter, et al., Phys. Rev. B 93 (2016) 014434.
[22] H.L. Feng, Z. Deng, C.U. Segre, M. Croft, S.H. Lapidus, C.E. Frank, Y. Shi, C. Jin, D. Walker, M. Greenblatt, Inorg. Chem. 60 (2021) 1241.
[23] W.T. Fu, R.J. Götz, D.J.W. IJdo, J. Solid State Chem. 183 (2010) 419.
[24] S.V. Haritha, Investigation of some 4d and 5d transition metal based Double Perovskites (Master's thesis), Indian Institute of Science Education and Research Pune, 2020.
[25] K.K. Wolff, L.H. Tjeng, M. Jansen, The new ordered double perovskite $SrLaCuIrO_6$, Solid State Commun. 289 (2019) 43.
[26] A.C. Larson, R.B. Von Dreele, General structure analysis system - GSAS/EXPGUI, Los Alamos National Laboratory Report No. LAUR 86-748, 2000; B. H. Toby. $EXPGUI$, a graphical user interface for $GSAS$, J. Appl. Crystallogr. 34 (2001) 210.
[27] G. Kresse, J. Furthmüller, Efficient iterative schemes for ab initio total-energy calculations using a plane-wave basis set, Phys. Rev. B 54 (1996) 11169.
[28] G. Kresse, D. Joubert, From ultrasoft pseudopotentials to the projector augmented-wave method, Phys. Rev. B 59 (1999) 1758.
[29] J.P. Perdew, K. Burke, M. Ernzerhof, Generalized gradient approximation made simple, Phys. Rev. Lett. 77 (1996) 3865.
[30] S.L. Dudarev, G.A. Botton, S.Y. Savrasov, C.J. Humphreys, A.P. Sutton, Electron-energy-loss spectra and the structural stability of nickel oxide: An LSDA+U study, Phys. Rev. B 57 (1998) 1505.
[31] M. Musa Saad H-E, A.K. Abdelhalim, et al., DFT and DFT+ U investigation of the effect of spin–orbit interaction and exchange–correlation energy on electronic and magnetic structures of Ir-based double perovskites Ba2TIrO6 (T=Cr, Mn, and Fe), AIP Adv. 10 (2020) 035306.
[32] S.R. Bhandari, S. Kc, S. Lawaju, R.K. Thapa, G.C. Kaphle, M.P. Ghimire, Electronic structure and estimation of Curie temperature in Ca2BIrO6 (B=Cr, Fe) double perovskites, J. Appl. Phys. 130 (2021) 175101.
[33] D.M. Ceperley, B.J. Alder, Phys. Rev. Lett. 45 (1980) 566.
[34] N. Artrith, J.A. Garrido Torres, A. Urban, M.S. Hybertsen, Data-driven approach to parameterize scan+u for an accurate description of 3d transition metal oxide thermochemistry, Phys. Rev. Mater. 6 (2022) 035003.
[35] Nicola A. Jordan, Peter D. Battle, Jeremy Sloan, Pascal Manuel, Susan Kilcoyne, Structural chemistry and magnetic properties of 6H and 15R hexagonal perovskites $BaIr_xFe_{1-x}O3_{3-\delta}$, J. Mater. Chem. 13 (2003) 2617–2625.
[36] A. Revelli, M. Moretti Sala, G. Monaco, M. Magnaterra, J. Attig, L. Peterlini, T. Dey, A.A. Tsirlin, P. Gegenwart, T. Fröhlich, M. Braden, C. Grams, J. Hemberger, P. Becker, D.I. Khomskii P.H.M. van Loosdrecht, J. van den Brink, M. Hermanns, M. Grüninger, Quasimolecular electronic structure of the spin-liquid candidate $Ba_3InIr_2O_9$, Phys. Rev. B 106 (2022) 155107.
[37] Michael W. Lufaso, Hans-Conrad zur Loye, Crystal structures and magnetic properties of mixed iridium-ruthenium triple perovskites. 2. $Ba_3MRuIrO_9$ (M=Li, Na, Mg, Ni, Zn, Bi, In), Inorg. Chem. 44 (2005) 9154–9161, 25.
[38] P. Beran, S.A. Ivanov, P. Nordblad, S. Middey, A. Nag, D.D. Sarma, S. Ray, R. Mathieu, Neutron powder diffraction study of $Ba_3ZnRu_{2-x}Ir_xO_9$ (x = 0, 1, 2) with 6H-type perovskite structure, Solid State Sci. 50 (2015) 58–64.
[39] Toru Yamashita, Peter Hayes, Analysis of XPS spectra of Fe^{2+} and Fe^{3+} ions in oxide materials, Appl. Surf. Sci. 254 (2008) 2441–2449.
[40] A.P. Grosvenor, B.A. Kobe, M.C. Biesinger, N.S. McIntyre, Investigation of multiplet splitting of fe 2p XPS spectra and bonding in iron compounds, Surf. Interface Anal. 36 (2004) 1564–1574.

[41] Wang Hay Kan, Min Chen, Jong-Seong Bae, Bok-Hee Kim, Venkataraman Thangadurai, Determination of fe oxidation states in the b-site ordered perovskite-type $Ba_2Ca_{0.67}Fe_{0.33}NbO_{6-\delta}$ at the surface (nano-scale) and bulk by variable temperature xps and tga and their impact on electrochemical catalysis, J. Mater. Chem. A 2 (2014) 8736.
[42] Hossein Fadaei, Carl Brown, Georges Houlachi, Houshang Alamdari, Iridium-based perovskites as efficient oxygen evolution reaction catalysts in acid media, ACS Appl. Eng. Mater. 2 (2024) 659–671.
[43] Yuqing Cheng, Yibo wang, Zhaoping Shi, Hongxiang Wu, Jiahao Yang, Jing Ni, Ming Yang, Ziang Wang, Meiling Xiao, Changpeng Liu, Wei Xing, Recent progress in advanced design of iridium-based and ruthenium-based perovskite catalysts for acidic oxygen evolution reaction, EcoEnergy 3 (1) (2025) 131–155.
[44] Paula Kayser, Jose A. Alonso, Federico J. Mompeán, Maria Retuerto, Mark Croft, Alexander Ignatov, Maria T. Fernández-Díaz, Crystal and magnetic structure of Sr_2BIrO_6 (B=Sc, Ti, Fe, Co, In) in the framework of multivalent iridium double perovskites, Eur. J. Inorg. Chem. 2015 (30) (2015) 5027–5038.
[45] Roumita Roy, Sudipta Kanungo, First principles investigation of spin–orbit coupling driven magnetism of the $3d-5d$ double-perovskite $(Sr/Ca)_2FeIrO_6$, Phys. Rev. B 106 (2022) 125113.
[46] K.C. Kharkwa, Roumita Roy, Harish Kumar, A.K. Bera, S.M. Yusuf, A.K. Shukla, Kranti Kumar, Sudipta Kanungo, A.K. Pramanik, Structure and magnetism and electronic properties in $3d-5d$ based double perovskite $(Sr_{1-x}Ca_x)_2FeIrO_6$ ($0 \leq x \leq 1$), Phys. Rev. B 102 (2020) 174401.
[47] Y. Yasukawa, J. Lindén, T.S. Chan, R.S. Liu, H. Yamauchi, M. Karppinen, Iron valence in double-perovskite $(Ba,Sr,Ca)_2FeMoO_6$: isovalent substitution effect, J. Solid State Chem. 177 (2004) 2655–2662.
[48] N. Nguyen, F. Sriti, C. Martin, F. Bourée, J.M. Grenèche, A. Ducouret, F. Studer, B. Raveau, Electronic distribution in the Ba_2FeMoO_6 double perovskite; the A-site size effect, J. Phys. : Condens. Matter 14 (2002) 12629.
[49] S. Agrestini, K. Chen, C.-Y. Kuo, L. Zhao, H.-J. Lin, C.-T. Chen, A. Rogalev, P. Ohresser, T.-S. Chan, S.-C. Weng, et al., Nature of the magnetism of iridium in the double perovskite Sr_2CoIrO_6, Phys. Rev. B 100 (2019) 014443.
[50] G. Cao, T.F. Qi, L. Li, J. Terzic, S.J. Yuan, L.E. DeLong, G. Murthy, R.K. Kaul, Novel magnetism of Ir^{5+} ($5d^4$) ions in the double perovskite Sr_2YIrO_6, Phys. Rev. Lett. 112 (2014) 056402.
[51] Klaus K. Wolff, Liu Hao Tjeng, Martin Jansen, Solid State Commun. 289 (2019) 43–46.
[52] Loi T. Nguyen, Tai Kong, R.J. Cava, Trimers of MnO_6 octahedra and ferrimagnetism of $Ba_4NbMn_3O_{12}$, Mater. Res. Express 6 (2019) 056108.
[53] N.W. Ashcroft, N.D. Mermin, Solid State Physics, Cengage Learning, New York, 2011.
[54] A. El Abed, E. Gaudin, J. Darriet, M.-H. Whangbo, Magnetic susceptibility and spin exchange interactions of the hexagonal perovskite-type oxides $Sr_{4/3}(Mn_{2/3}Ni_{1/3})O_3$, J. Solid State Chem. 163 (2002) 513–518.
[55] S. Mugiraneza, A.M. Hallas, Tutorial: a beginner's guide to interpreting magnetic susceptibility data with the Curie–Weiss law, Commun. Phys. 5 (2022) 95.
[56] J.A. Mydosh, Spin Glasses: An Experimental Introduction, Taylor & Francis, London, 1993.
[57] J. Souletie, J.L. Tholence, Critical slowing down in spin glasses and other glasses: Fulcher versus power law, Phys. Rev. B 32 (1985) 516.
[58] T. Elovaara, H. Huhtinen, S. Majumdar, P. Paturi, Linear and nonlinear ac susceptibilities in polycrystalline low-bandwidth $Pr_{1-x}Ca_xMnO_3$ (x=0.0–0.3) manganite, J. Phys. : Condens. Matter 26 (2014) 266005.
[59] Haiying He, Zhihao Yang, Yonghang Xu, Andrew T. Smith, Guangguang Yang, Luyi Sun, Perovskite oxides as transparent semiconductors: a review, Nano Converg. 7 (2020) 32.
[60] D. Serrate, J.M. De Teresa, M.R. Ibarra, Double perovskites with ferromagnetism above room temperature, J. Phys. : Condens. Matter. 19 (2007) 023201.
[61] V.M. Goldschmidt, Die gesetze der krystallochemie, Naturwissenschaften 14 (1926) 477–485.
[62] R.D. Shannon, Revised effective ionic radii and systematic studies of interatomic distances in halides and chalcogenides, Acta Cryst. A 32 (1976) 751.
[63] M.J. Swamynadhan, Gwan Yeong Jung, Pravan Omprakash, Rohan Mishra, Design rules and discovery of face-sharing hexagonal perovskites, Chem. Mat. 38 (4) (2026) 1679–1688.